

# High-resolution light field prints by nanoscale 3D printing

**Authors:** John You En Chan <sup>1</sup>, Qifeng Ruan <sup>1\*</sup>, Menghua Jiang <sup>2</sup>, Hongtao Wang <sup>1</sup>, Hao Wang <sup>1</sup>, Wang Zhang <sup>1</sup>, Cheng-Wei Qiu <sup>2</sup>, Joel K.W. Yang <sup>1,3\*</sup>

<sup>1</sup> Engineering Product Development, Singapore University of Technology and Design, Singapore 487372.

<sup>2</sup> Department of Electrical and Computer Engineering, National University of Singapore, Singapore 117583.

<sup>3</sup> Institute of Materials Research and Engineering, Singapore 138634.

\* To whom correspondence should be addressed. Email: [qifeng\\_ruan@sutd.edu.sg](mailto:qifeng_ruan@sutd.edu.sg); [joel\\_yang@sutd.edu.sg](mailto:joel_yang@sutd.edu.sg)

## **Abstract**

A light field print (LFP) displays three-dimensional (3D) information to the naked-eye observer under ambient white light illumination. Changing perspectives of a 3D image are seen by the observer from varying angles. However, LFPs appear pixelated due to limited resolution and misalignment between their lenses and colour pixels. A promising solution to create high-resolution LFPs is through the use of advanced nanofabrication techniques. Here, we use two-photon polymerization lithography as a one-step nanoscale 3D printer to directly fabricate LFPs out of transparent resin. This approach produces simultaneously high spatial resolution (29 – 45  $\mu\text{m}$ ) and high angular resolution ( $\sim 1.6^\circ$ ) images with smooth motion parallax across  $15 \times 15$  views. Notably, the smallest colour pixel consists of only a single nanopillar ( $\sim 300$  nm diameter). Our LFP signifies a step towards hyper-realistic 3D images that can be applied in print media and security tags for high-value goods.

Commonly available prints have a fixed two-dimensional (2D) appearance as they store only intensity and colour information. Unfortunately, these prints lack a vital piece of information – the directional control of light rays<sup>1-4</sup> – to display a three-dimensional (3D) image. With no ability to discriminate the direction of light rays, the prints appear unchanged to an observer from all viewing angles. On the other hand, light field prints (LFPs) encode directional information, which enables them to display changing perspectives of a 3D image seen from varying viewing angles. This technique of displaying a 3D image was discovered in 1908 by the Nobel Laureate, Gabriel Lippmann<sup>5</sup>. He proposed using an array of tiny lenses on film to record a scene, so that each lens formed its own sub-image with a slightly shifted perspective. The film would then be illuminated under diffuse light to reconstruct an integral 3D image of the scene. LFPs are autostereoscopic as their 3D images are visible to the naked eye under incoherent and unpolarized illumination, which gives them an advantage over stereoscopic prints<sup>6,7</sup> that require viewing through a pair of anaglyph glasses or orthogonally polarized filters. LFPs also do not require laser illumination used in conventional holograms<sup>8</sup>. However, LFPs appear pixelated because of low spatial resolution and low angular resolution caused by fabrication limitations. Spatial resolution is limited by the centre-to-centre separation between lenses, and angular resolution is limited by the density of pixels under each lens<sup>9,10</sup>.

To create high-resolution LFPs, we leverage on advanced nanofabrication techniques in structural colour printing<sup>11-24</sup>. Structural colour prints with plasmonic nanostructures<sup>16,18</sup> can attain a pixel resolution of  $\sim 100,000$  dots per inch, which is several orders of magnitude higher than that of conventional inkjet prints<sup>17</sup>. Though inkjet printers are capable of printing LFPs for art<sup>25</sup>, their pixel resolution is insufficient for optical security devices<sup>26</sup> that require the spatial resolution to be  $< 50 \mu\text{m}$  (*i.e.* beyond the resolving power of human vision). Moreover, misregistration between colour layers is an issue in these printers, but not in nanofabrication tools such as electron beam lithography that position plasmonic colour pixels without misregistration<sup>14</sup>. Jiang et. al. demonstrated high-resolution multi-colour motion effects by bonding a microlens array onto a plasmonic colour print<sup>27</sup>. However, this approach is relatively complicated because it requires multiple processing steps and manual alignment between the microlenses and pixels. Accurate alignment is essential to reconstruct clear 3D images but doing manual alignment at the nanoscale is

challenging as it relies on delicate movements and visual inspection. As manual alignment has been done for regular arrays of microlenses and colour pixels, an alternative alignment approach is thus needed for irregular arrays.

Here, we used two-photon polymerization lithography (TPL) to fabricate high-resolution LFPs in one patterning step that circumvents the need for doing manual alignment. The microlenses and structural colour pixels of our LFPs were aligned automatically in the TPL system (Nanoscribe GmbH Photonic Professional GT system), which can position each volumetric pixel exposed by the laser up to an accuracy of 10 nm. As TPL is an additive manufacturing technology, the microlenses and structural colour pixels were fabricated in discrete slicing height steps of 20 nm and 300 nm respectively. The microlenses and structural colour pixels were made of the same low refractive index material, IP-Dip photoresist ( $n \sim 1.55$ ). Unlike plasmonic colour pixels, our structural colour pixels do not require additional metal deposition, which makes the TPL system only necessary for fabricating LFPs. The microlenses and structural colour pixels were fabricated together in a pseudorandom arrangement to minimize moiré patterns caused by the superposition of regular arrays<sup>28</sup>. A pseudorandom arrangement can also be used to encode secret information for security applications. More importantly, our LFP displayed high spatial resolution (29  $\mu\text{m}$  – 45  $\mu\text{m}$ ) and high angular resolution ( $\sim 1.6^\circ$ ) images with smooth motion parallax that appeared unpixellated to the naked eye, even up close.

## Results

### Design concepts

We propose the working principle of our light field print (LFP): A white light source is used to illuminate the structural colour pixels, which function as colour filters that transmit varying intensities of visible wavelengths within a range of angles collected by the microlenses. The microlenses then project the collected light to an observer who sees the colours of selected pixels at the corresponding viewpoint in the far field. All these selected pixels form a complete 3D image (Fig. 1a). The design of our LFP was inspired by Thiele et. al.'s compound microlens system<sup>29</sup>. Instead of a compound system, we designed our system (Fig. 1b) with a hollow tower to support a spherical plano-convex microlens above a block of structural colour pixels that contains an array

of nanopillars<sup>8,30,31</sup>. We refer to this system as a display unit. Our LFP comprised  $65 \times 65$  display units placed in a pseudorandom arrangement with centre-to-centre separation between  $29 \mu\text{m} - 45 \mu\text{m}$ . A centre-to-centre separation  $< 50 \mu\text{m}$  ensured that the 3D image appeared unpixellated to the naked eye. In each display unit, the tower was constructed with several openings to allow uncured photoresist to be washed away after printing. The tower had height =  $34.6 \mu\text{m}$  and diameter =  $26 \mu\text{m}$ , whereas the microlens had radius of curvature  $R = 22 \mu\text{m}$  and diameter  $L = 21 \mu\text{m}$ . Each microlens was placed one focal length  $\sim 37 \mu\text{m}$  above the structural colour pixels to obtain a focused image (see Raytracing simulations). The diameter and focal length of our microlens corresponded to a numerical aperture ( $NA$ ) of  $\sim 0.28$ , designed to cover an acceptable range of viewing angles ( $\phi = 0^\circ$  to  $16^\circ$ ) that was limited by our structural colour pixels (see Electromagnetic wave simulations). This  $NA$  yielded a diffraction-limited focal spot size of  $\sim 1 \mu\text{m}$ , which equalled the smallest pixel pitch  $P$  in our design. Initially, we designed  $3 \times 3$  pixels per display unit. Each pixel comprised  $5 \times 5$  nanopillars ( $P = 5 \mu\text{m}$ ) with diameter  $D$ , height  $H$  and pitch  $S$  (Fig. 1c). Subsequently, we increased the number of pixels per display unit to  $5 \times 5$  pixels ( $P = 3 \mu\text{m}$ ,  $3 \times 3$  nanopillars per pixel) and  $15 \times 15$  pixels ( $P = 1 \mu\text{m}$ , single nanopillar per pixel). In every display unit, the block of pixels fits within the circular cross-section of the microlens (Fig. 1d). The number assigned to each square represents a pixel extracted from an input image with that number, e.g. a pixel labelled '1' is extracted from the first input image. Hence, the number of pixels per display unit equals the number of input images. We generated 9 input images of a multi-coloured cube with different perspectives, and used an algorithm<sup>32</sup> to create an interlaced digital image that maps the pixel positions to their display units. Note that the order of numbers assigned to the input images is flipped horizontally and vertically from the order of numbers assigned to the pixels (equivalent to a  $180^\circ$  rotation about the optical axis). This order ensured that the LFP displayed a 3D image with proper depth and motion parallax, otherwise it would appear pseudoscopic (*i.e.* depth-inverted)<sup>9,33</sup>. In the design process, we performed raytracing simulations to determine the microlens focal length and acceptable range of viewing angles. We also performed full electromagnetic wave simulations to determine the microlens focal spot size and the colour change of pixels with viewing angle.

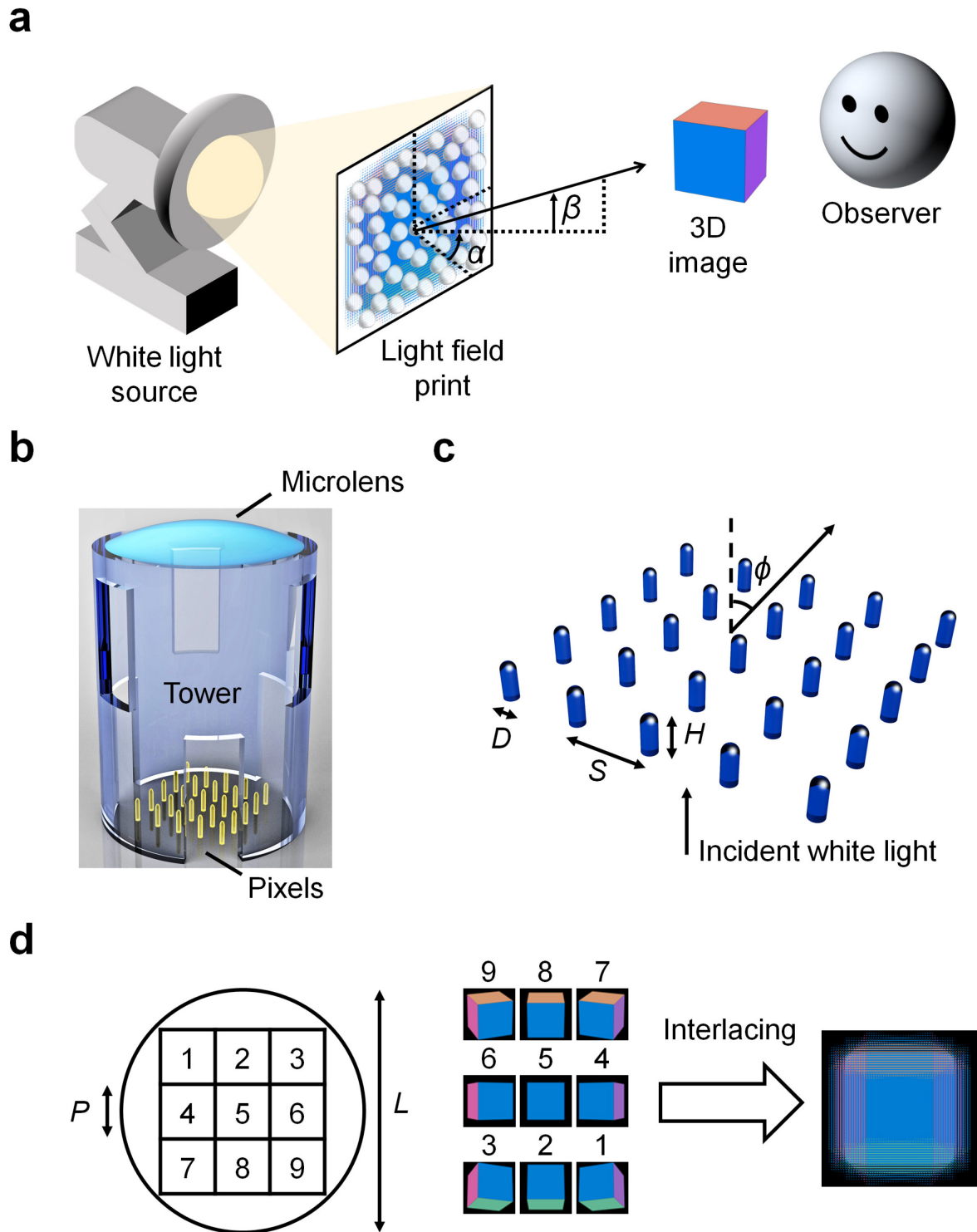


**Figure 1.** (a) Schematic that illustrates the working principle of our light field print (LFP). A white light source is used to illuminate the structural colour pixels in the LFP. Transmitted light from the pixels is collected by the microlenses and projected to the far-field. An observer in the far-field sees a colourful 3D image from the viewpoint denoted by azimuthal angle  $\alpha$  and elevation angle  $\beta$ . (b) Schematic of one display unit: A tower supports a spherical plano-convex microlens placed one focal length above a block of structural colour pixels that

contains an array of nanopillars. (c) Schematic of one structural colour pixel that contains  $5 \times 5$  nanopillars, in which each nanopillar has diameter  $D$ , height  $H$  and pitch  $S$ .  $\phi$  is the viewing angle of the pixel. (d) (Left) Plan-view schematic of  $3 \times 3$  pixels in a display unit.  $L$  is the diameter of the microlens, represented by a circle;  $P$  is the pitch of each pixel, represented by a square. Each pixel is assigned a number 1 – 9 and it is extracted from an input image assigned with the same number. (Right) The input images are interlaced to generate a digital map of pixel positions for printing the LFP.

### Raytracing simulations

As our structural colour pixels had a limited acceptable range of viewing angles ( $\phi = 0^\circ$  to  $16^\circ$ ), they required microlenses with numerical aperture  $\sim 0.28$ . To fulfil this requirement, we designed spherical plano-convex microlenses with diameter  $L = 21 \mu\text{m}$  and radius of curvature  $R = 22 \mu\text{m}$ . From the lens-maker equation, we derived the theoretical focal length of our microlenses to be  $F' = 40 \mu\text{m}$  for refractive index  $n = 1.55$ . The theoretical focal length is expressed in Equation 1:

$$F' = \frac{R}{n - 1} \quad (1)$$

To validate our design, we simulated parallel incident light rays on the convex side of the microlens for field angle  $\theta = 0^\circ$  and sampling wavelengths  $\lambda = \{450, 532, 635\}$  nm (Supplementary Note 1). We refer to field angle as the angle between the incident ray and optical axis. For the respective wavelengths, we set  $n = \{1.56, 1.55, 1.54\}$  according to the Cauchy parameters of UV cured IP-Dip photoresist<sup>34</sup>. After accounting for aberrations, we found that the focal plane of the microlens was located at  $\sim z = 37 \mu\text{m}$  below its vertex (Fig. 2a). We used this value as our design focal length  $F$ , which is in close agreement with  $F'$ . Based on the principle of reversibility of light, we designed the structural colour pixels at this focal plane, so that transmitted light from the pixels would emerge as parallel rays into the far field. Our microlens showed spherical aberration and chromatic aberration. In geometric optics<sup>35</sup>, spherical aberration is caused by the spherical microlens which focuses marginal rays and paraxial rays at different points along the optical axis, whereas chromatic aberration is caused by the dispersion of the material due to its wavelength-dependent refractive index. At  $\theta = 16^\circ$  (Fig. 2b), we found that the focal plane shifted in the negative  $z$ -direction due to another aberration known as field curvature, which causes light rays with different field angles ( $\theta \geq 0^\circ$ ) to focus on a curved surface rather than on a flat

plane. Despite the presence of aberrations, the microlens behaves as intended: an optical router<sup>31</sup> that directs light rays from selected pixel positions to the observer. In the thin lens approximation, the pixel's position selected by the microlens is expressed in Equation 2:

$$x = F \tan \theta \quad (2)$$

For a given field angle  $\theta$ , the microlens forms a focal spot at position  $x$ . As a change in  $\theta$  leads to a change in  $x$ , the set of light rays focused by the microlens translates across different pixel positions. This translation mechanism enables the microlens to steer the direction of light rays and display changing perspectives of a 3D image at their corresponding viewpoints.

### Electromagnetic wave simulations

To evaluate the microlens focal spot size, which determined the smallest pixel pitch in our LFP, we simulated the electric field intensity distributions of the focal spot on the plane  $z = 37 \mu\text{m}$ , for field angle  $\theta = 0^\circ$  and wavelengths  $\lambda = \{450, 532, 635\} \text{ nm}$ . We then calculated the full width at half maximum (*FWHM*) of the electric field intensity profile of the horizontal slice at  $y = 0$  (Fig. 2c). For the respective wavelengths, the  $FWHM = \{0.85, 1.00, 1.19\} \mu\text{m}$ , which are in close agreement with their own diffraction-limited value ( $FWHM'$ ) expressed in Equation 3.

$$FWHM' = 0.51 \frac{\lambda}{NA} \quad (3)$$

where  $\lambda$  is the wavelength of light, and  $NA$  is the microlens numerical aperture. On the same plane  $z = 37 \mu\text{m}$ , we also simulated how the *FWHM* changed from  $\theta = 0^\circ$  to  $16^\circ$  for the respective wavelengths. The plot of *FWHM* vs.  $\theta$  revealed an overall increasing trend (Fig. 2d), which suggests that image defocus becomes more severe at larger field angles. This trend is expected for a single lens element that is uncorrected for aberrations.

Based on the simulation results of our microlens, we designed our initial pixel pitch ( $P = 5 \mu\text{m}$ ) to be larger than the *FWHM*. Our initial pixel comprised  $5 \times 5$  nanopillars, in which each nanopillar has diameter  $D$ , height  $H$  and pitch  $S$  (Fig. 1c). Though these nanopillars have previously been shown to produce a wide range of colours<sup>8,30,31</sup>, their colour change with viewing angle has not yet been characterized. To simulate a representative pixel, we set  $D = 0.3 \mu\text{m}$ ,  $H = 1.2 \mu\text{m}$ ,  $S = 1 \mu\text{m}$ , and calculated its

transmittance spectra for different viewing angles  $\phi$  (Fig. 2e). From  $\phi = 0^\circ$  to  $8^\circ$ , the shape of the spectra remained unchanged. However, from  $\phi = 8^\circ$  to  $16^\circ$ , the trough of the spectra shifted from 570 nm to 586 nm and increased its transmittance from 3 % to 12 %, which suggests that the spectral contrast and saturation are reduced at larger viewing angles. Hence, the numerical aperture of our microlens ( $NA \sim 0.28$ ) was optimal for our structural colour pixels, as it covered an acceptable range of viewing angles from  $\phi = 0^\circ$  to  $16^\circ$ . Within this range of angles, we expect to see minimal colour change in any pixel, or in the image of the LFP.

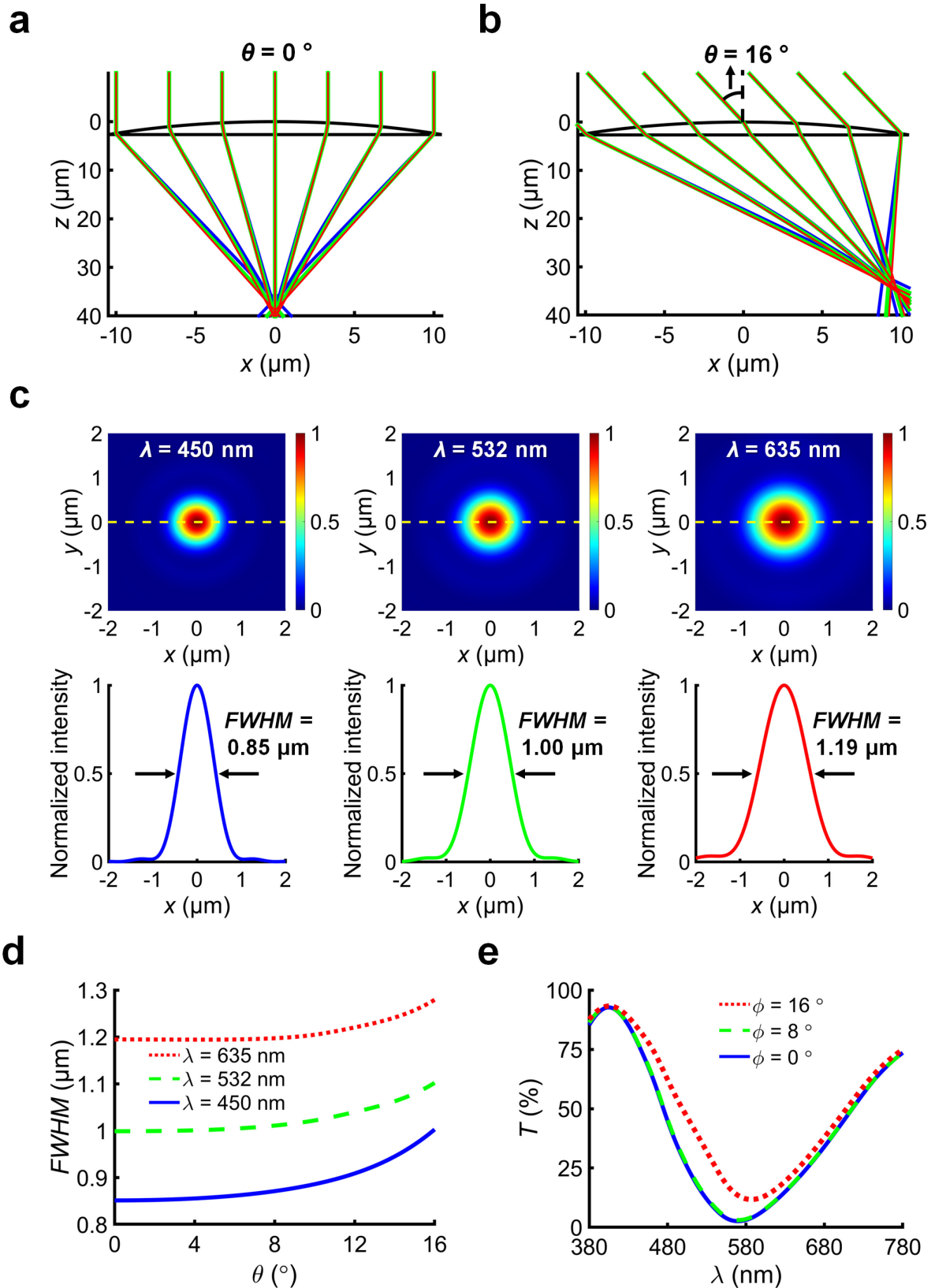


**Figure 2.** (a – b) Raytracing simulation of the microlens for field angles  $\theta = \{0, 16\}^\circ$  that select the centre and corner pixel positions respectively. (c) Simulated normalized electric field intensity distribution of the focal spot on the plane  $z = 37 \mu\text{m}$ , for  $\theta = 0^\circ$  and wavelengths  $\lambda = \{450, 532, 635\}$  nm respectively. The focal spot size was calculated as the full width at half

maximum (*FWHM*) of the normalized electric field intensity profile of the horizontal slice  $y = 0$ , indicated by the yellow dashed line. (d) Plot of the simulated *FWHM* vs.  $\theta$  for the respective wavelengths. (e) Simulated transmittance spectra of a representative pixel (which comprised  $5 \times 5$  nanopillars with diameter  $D = 0.3 \mu\text{m}$ , height  $H = 1.2 \mu\text{m}$ , pitch  $S = 1 \mu\text{m}$ ) for viewing angles  $\phi = \{0, 8, 16\}^\circ$ .

### **Fabrication and observation**

We fabricated our LFP by two-photon polymerization lithography of IP-Dip photoresist on a glass substrate. To create a wide range of structural colour pixels, we varied the height of nanopillars from  $0.6 \mu\text{m}$  and  $2.7 \mu\text{m}$  in steps of  $0.3 \mu\text{m}$ , and the laser exposure time from  $0.04 \text{ ms}$  to  $0.32 \text{ ms}$  in steps of  $0.04 \text{ ms}$  per exposed voxel. The laser exposure time controlled the diameter of nanopillars. All nanopillars were exposed by femtosecond laser pulses, with the laser power set to  $20 \text{ mW}$ . We then measured the transmittance spectra of the structural colour pixels and plotted their coordinates on the CIE chromaticity diagram (Supplementary Fig. 1 and Supplementary Note 2). We used the CIE data to map the structural colour pixels of our LFP to their patterning parameters. To reduce printing time, the laser scanned only the surface shell of the towers and microlenses. Uncured photoresist within the shell was later solidified by UV curing<sup>36</sup>. The display units were fabricated in a pseudorandom arrangement, such that the centre-to-centre separation between adjacent display units ranged from  $29 \mu\text{m} - 45 \mu\text{m}$  in  $x$  and  $y$  directions. Under an optical microscope, the display units of our LFP looked like colourful compound eyes as found in insects (Fig. 3a). Though each display unit comprised a microlens and a block of pixels with multiple colours, a bright single-colour spot was produced when the optical microscope was focused at the front focal plane of the display unit. This bright single-colour spot was caused by the mixing of different wavelengths of light from pixels under each microlens (Supplementary Fig. 2).

To demonstrate the colour mixing effect, we fabricated a display unit and a block of pixels next to each other on a separate substrate. We designed the pixels with equal areas of red, blue, and green stripes. The same pixels were patterned beneath the microlens of the display unit. When the optical microscope was focused on the pixels, the stripes were clearly resolved (Fig. 3b). However, when the optical microscope was focused on the front focal plane of the display unit, the stripes became out-of-focus,

and a bright white spot was formed above the display unit (Fig. 3c). The spot appeared white because the stripes had equal areas, so the colour of each stripe contributed in equal proportion to the total spectral power distribution of the spot. Hence, larger areas of pixels with the same colour will contribute a larger proportion to the total spectral power distribution and influence the resultant colour of the spot. We also fabricated  $2 \times 2$  display units to examine their structure under a scanning electron microscope (SEM) (Fig. 3d). As the microlenses were printed at a discrete slicing height step of 20 nm, their layering artefacts are visible in the SEM image. Despite the presence of layering artefacts, the microlenses still showed good optical performance. To test the microlens performance, we used a laser setup to capture focal spot images for central wavelengths  $\lambda = \{450, 532, 635\}$  nm (Supplementary Fig. 3). In each focal spot image, we measured the intensity distribution of its centre horizontal slice, then calculated the  $FWHM = \{0.88, 1.03, 1.21\}$   $\mu\text{m}$  and Strehl ratio =  $\{0.88, 0.88, 0.89\}$  for the respective wavelengths. The Strehl ratio was calculated by normalizing the intensity distribution of the horizontal slice with same area under the curve as an ideal Airy disk function<sup>37</sup>. A Strehl ratio  $> 0.8$  suggests that the microlens performance approaches the diffraction limit. We fabricated another  $3 \times 3$  structural colour pixels to examine their nanopillars under the SEM (Fig. 3e). Each pixel comprised  $5 \times 5$  nanopillars with the same height and diameter. The pixels are distinguishable from one another in the SEM image, as adjacent pixels have different heights and diameters of nanopillars. Due to the similar structure of nanopillars in each pixel, its colour appeared uniform under the optical microscope.

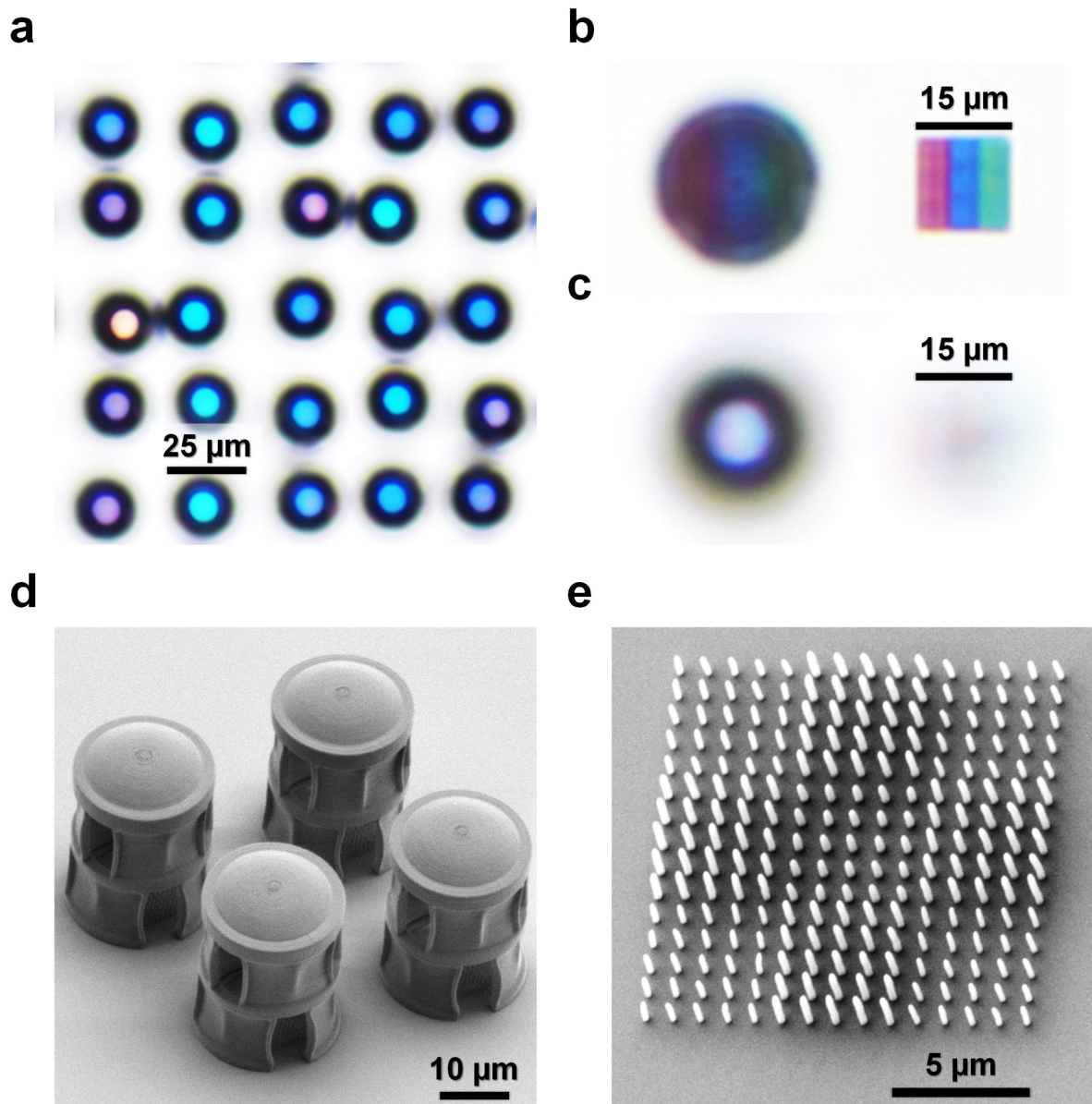


**Figure 3.** (a) Brightfield transmission optical microscope image (plan-view) of the display units in a pseudorandom arrangement. (b – c) Brightfield transmission optical microscope images of a display unit (left) and a block of structural colour pixels designed with red, blue, and green stripes (right). The same pixels were patterned beneath the microlens of the display unit. (b) The optical microscope image was focused on the pixels. (c) The optical microscope image was focused on the front focal plane of the display unit. (d) Scanning electron microscope (SEM) image (45 ° tilt angle) of 2 × 2 display units. (e) SEM image (30 ° tilt angle) of 3 × 3 pixels, in which each pixel is recognizable by 5 × 5 nanopillars with the same height and diameter.

Next, we used a white light-emitting diode lamp to illuminate our LFP and observed it from several viewpoints in the far field. The viewpoints are indicated by azimuthal

angle  $\alpha = \{-8, 0, 8\}^\circ$  and elevation angle  $\beta = \{-8, 0, 8\}^\circ$  relative to the centre normal line of sight (Fig. 1a). We captured digital camera images of the LFP, which revealed different perspectives of the cube at different viewpoints (Fig. 4). These images have a grainy appearance as they were captured by the camera's macro lens that resolved individual microlenses in the LFP. However, the LFP appeared unpixelated to the naked eye as the centre-to-centre separation between microlenses ( $29\ \mu\text{m} - 45\ \mu\text{m}$ ) was smaller than the eye's resolving power ( $\sim 50\ \mu\text{m}$ ). We observed that the colours of the cube were consistent throughout the acceptable range of viewing angles ( $\phi = 0^\circ$  to  $16^\circ$ ), which agreed with our simulation results in Fig. 2e. When the camera was placed in between the specified viewpoints, we observed an image with different perspectives of the cube fused together, which we refer to as crosstalk (Supplementary Fig. 4). Crosstalk was caused by the position of the microlens focal spot on at least two adjacent structural colour pixels in each display unit. To avoid crosstalk, the focal spot should be smaller than one pixel and positioned within the area of any given pixel. As each pixel encoded a discrete perspective of the 3D object, the image transition between viewpoints was quasi-continuous, which gave an impression of motion parallax. Smoother motion parallax can be achieved by reducing pixel pitch and encoding the LFP with more input images that have smaller angular differences in perspective.

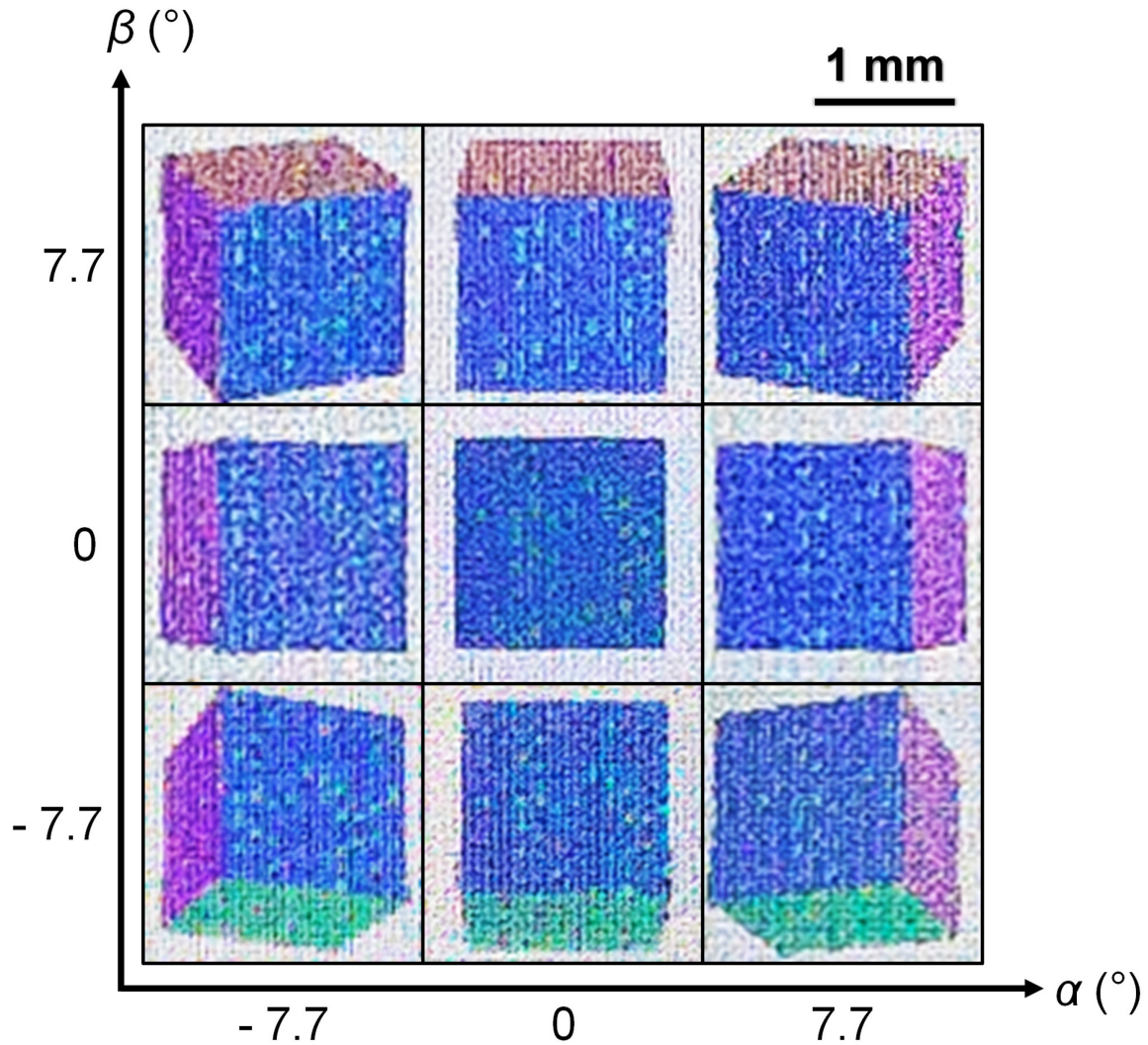


**Figure 4.** Digital camera macro images of a multi-coloured cube, taken from  $3 \times 3$  different viewpoints denoted by the azimuthal angle  $\alpha$  and the elevation angle  $\beta$ . In this light field print, each pixel comprised  $5 \times 5$  nanopillars (pixel pitch  $P = 5 \mu\text{m}$ ). The cube appeared to protrude out of the plane of the substrate.

#### **Effects of reducing pixel pitch**

To investigate how smaller pixel pitch affects image crosstalk and the smoothness of motion parallax, we fabricated another LFP in which each pixel comprised  $3 \times 3$  nanopillars. The pitch between nanopillars remained as  $S = 1 \mu\text{m}$ , but the pixel pitch was reduced to  $P = 3 \mu\text{m}$ . In designing the LFP, we used an open-source 3D model of a cartoon face (<http://objects.povworld.org/cgi-bin/dl.cgi?soldier.zip>) and computer graphics software (POV-Ray) to generate  $5 \times 5$  input images with different perspectives. We encoded each input image with a row number on the left side, and a column number on the right side. The row number increases from top to bottom

viewpoints, and the column number increases from left to right viewpoints. These numbers served as visual cues for us to position the camera at each specified viewpoint and avoid crosstalk when capturing images of the LFP. We followed the same design and fabrication process, and captured images of the LFP from different viewpoints (Fig. 5). Due to the larger number of input images, we found that these captured images of the cartoon face ( $P = 3 \mu\text{m}$ ) showed crosstalk at more transition viewpoints than the images of the cube ( $P = 5 \mu\text{m}$ ). However, the captured images of the cartoon face also showed smoother motion parallax than the images of the cube due to a smaller angular sampling interval of the LFP. The angular sampling interval  $\omega_a$  is expressed in Equation 4:

$$\omega_a = \tan^{-1}\left(\frac{P}{F}\right) \quad (4)$$

where  $P$  is the pixel pitch, and  $F$  is the microlens focal length. A smaller value of  $\omega_a$  indicates higher angular resolution and smoother motion parallax.

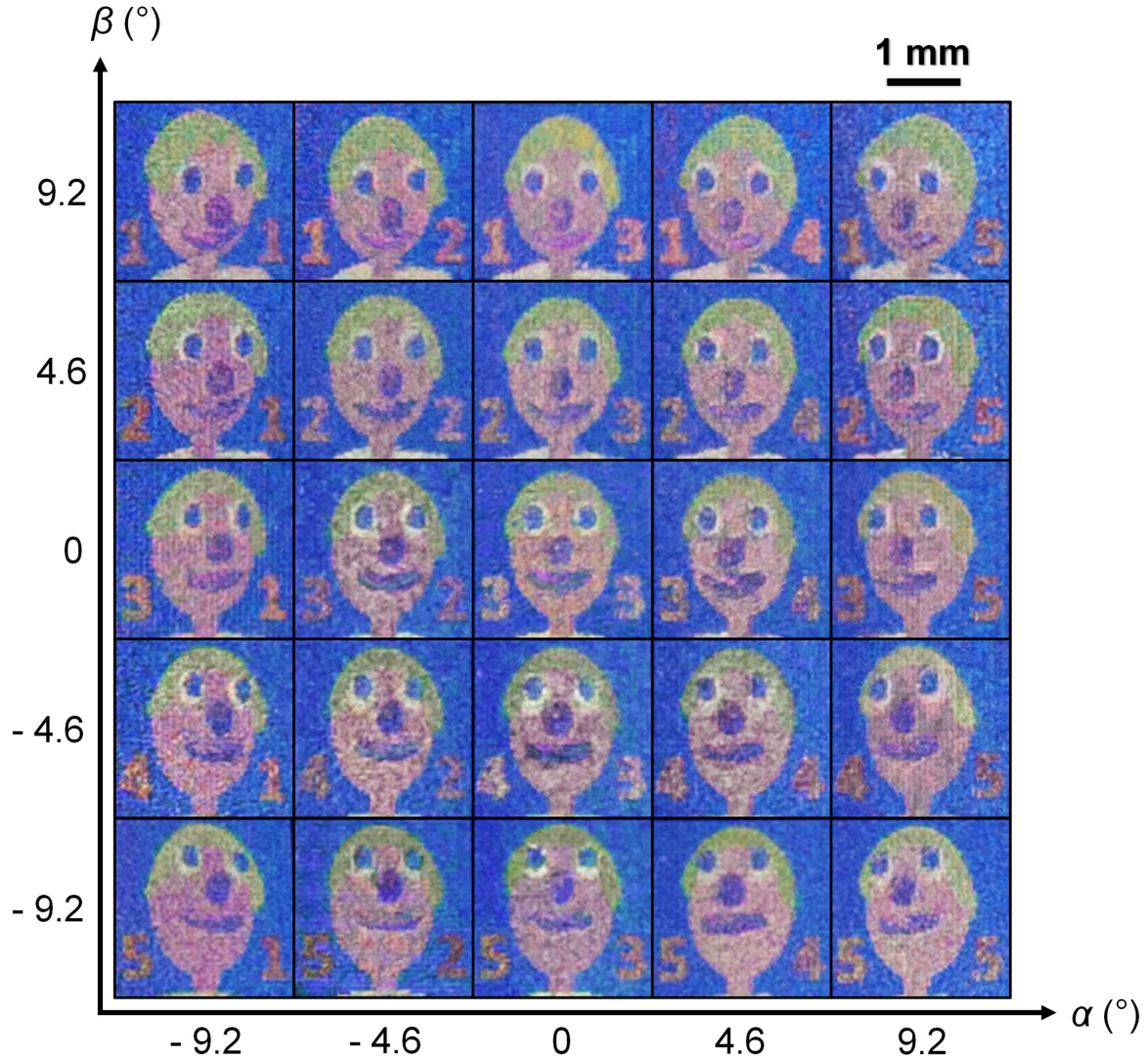


**Figure 5.** Digital camera macro images of a computer-generated cartoon face, taken from  $5 \times 5$  different viewpoints indicated by the azimuthal angle  $\alpha$  and the elevation angle  $\beta$ . In this light field print, each colour pixel comprised  $3 \times 3$  nanopillars (pixel pitch  $P = 3 \mu\text{m}$ ). The cartoon face appeared to protrude out of the plane of the substrate.

To determine the highest angular resolution of our LFP, we fabricated each pixel with only a single nanopillar ( $\sim 300 \text{ nm}$  diameter), which was the smallest printable feature size in our TPL system. This LFP was encoded with  $15 \times 15$  input images of the cartoon face and its pixel pitch was  $P = 1 \mu\text{m}$ , same as the pitch between nanopillars ( $S = 1 \mu\text{m}$ ). The area of the LFP spanned  $2 \text{ mm} \times 2 \text{ mm}$ . Remarkably, we still observed clear and colourful images with smooth motion parallax, as this result shows that a single nanopillar suffices to represent a colour pixel. We found that reducing the pixel size from  $5 \times 5$  nanopillars to only a single nanopillar had little effect on the appearance

of pixel colour and contrast (Supplementary Fig. 5). To achieve the smoothest motion parallax, we propose that the angular sampling interval ( $\omega_a$ ) and the angular difference in perspective between input images ( $\omega_b$ ) should be smaller than a threshold angle<sup>38</sup> expressed in Equation 5:

$$\delta = \tan^{-1} \left( \frac{E}{V} \right) \quad (5)$$

where  $\delta$  is the angle between two sampled light rays that enter the eye,  $E$  is the pupil diameter of the eye, and  $V$  is the viewing distance from the eye to the 3D image. If this condition is satisfied (*i.e.*  $\omega_a \leq \delta$  and  $\omega_b \leq \delta$ ), the eyes will perceive the smoothest motion parallax and resolve the accommodation-vergence conflict<sup>38-40</sup> (*i.e.* the experience of visual discomfort when the eyes focus on a different point from where they converge). For  $E = 6$  mm and  $V = 150$  mm (*i.e.* the close focusing distance of the naked eye),  $\delta = 2.3^\circ$ . Under close inspection, we observed images with smooth motion parallax because  $\omega_a$  ( $\sim 1.6^\circ$ ) and  $\omega_b$  ( $\sim 2.1^\circ$ ) were smaller than  $\delta$ . We also observed how the images transitioned smoothly by tilting the substrate horizontally and vertically, while fixing the position of the camera and light source (Supplementary Movie 1). As the substrate was tilted, the varying incident angle of light on the LFP caused variation in its image colour brightness and contrast. The image became white or translucent when the substrate was tilted beyond the largest acceptable viewing angle  $\sim 16^\circ$ , which caused the microlenses to select an area with no pixels on the substrate. We verified that the LFP formed a 3D image when we focused the camera on the microlenses (Fig. 6a) and slightly above the microlenses (Fig. 6b). The image appeared clearer in the latter case, which was closer to what we observed by naked eye. The images in Fig. 6 revealed the pixelated composition of the LFP as they were captured by the macro lens of the camera that resolved individual microlenses in the LFP. To mitigate the pixelated appearance of the image, the LFP can be fabricated with a larger total area and captured at reduced magnification. By using a simplified geometric model<sup>41</sup> (Supplementary Note 3), we calculated the maximum image depth to be 1.3 mm, which refers to how much the 3D image appeared to float above or sink below the LFP as seen from the centre viewpoint. The maximum image depth  $I$  is expressed in Equation 6:

$$I = \frac{CF}{P} \quad (6)$$

where  $C$  is the centre-to-centre separation distance of the microlens,  $F$  is the focal length of the microlens, and  $P$  is the pixel pitch. In the calculation of maximum image depth, we used an average  $C$  of  $37\ \mu\text{m}$ . Hence, the total depth range of the 3D image was  $1.3\ \text{mm} \times 2 = 2.6\ \text{mm}$ . Our LFP worked in transmission mode, where the light source and observer are on opposite sides of the glass substrate. The LFP can also work in reflection mode by adding a mirror on the clean side of the substrate and placing the light source on the same side as the observer. However, the image brightness and contrast were reduced in reflection mode (Supplementary Fig. 6) due to more light scattering and optical losses at the interfaces of the microlenses, which gave the LFP a washed-out appearance.

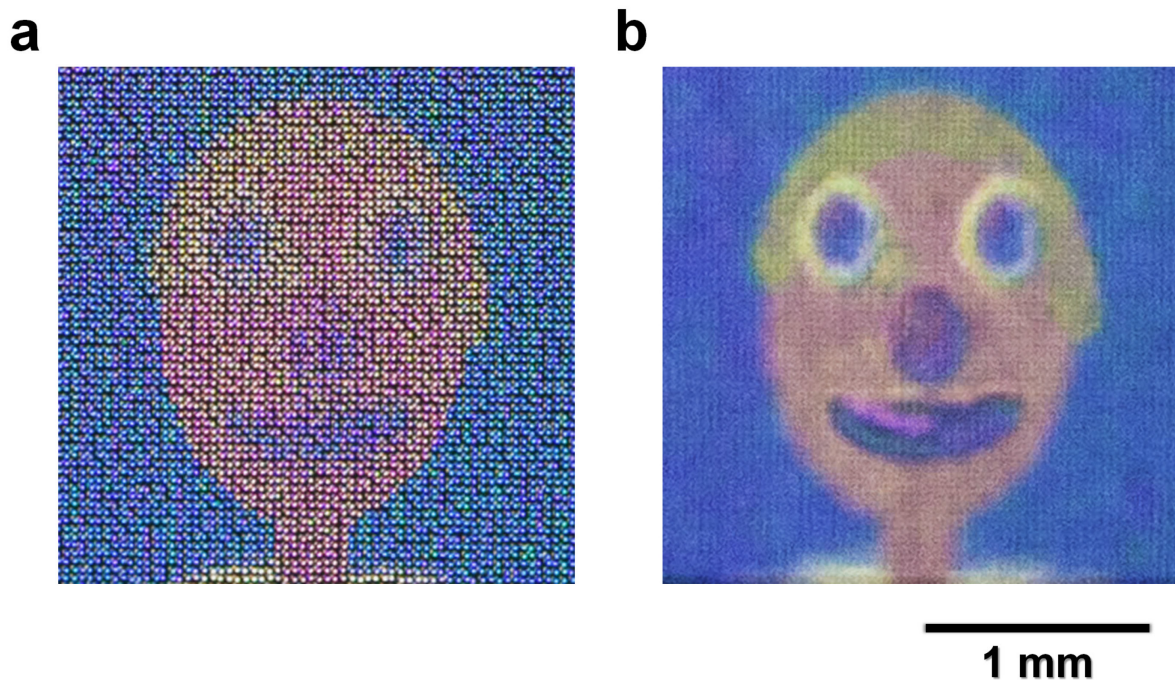


**Figure 6.** Digital camera macro images of the computer-generated cartoon face taken straight on from the central viewpoint (azimuthal angle  $\alpha = 0^\circ$  and elevation angle  $\beta = 0^\circ$ ). This light field print was encoded with  $15 \times 15$  input images, and each colour pixel comprised only a single nanopillar  $\sim 300\ \text{nm}$  diameter (pixel pitch  $P = 1\ \mu\text{m}$ ). (a) Image taken with the camera focused on the plane of the microlenses. (b) Image taken with the camera focused slightly in front of the microlenses, which also simulates what an observer sees.

## Discussion

We have presented a nanoscale 3D printing approach to directly fabricate high-resolution light field prints by two-photon polymerization lithography. Our fabrication process only involved patterning IP-Dip photoresist on a glass substrate and

developing the photoresist in chemical solution, along with UV curing. We fabricated plano-convex spherical microlenses with numerical aperture  $\sim 0.28$  and structural colour pixels with nanopillars, that were designed to display directional information across a range of viewing angles from  $0^\circ$  to  $16^\circ$ . We systematically reduced the size of each pixel from  $5 \times 5$  nanopillars to just a single nanopillar ( $\sim 300$  nm in diameter) and found that it still produced clear and colourful images with smooth motion parallax. By fabricating single nanopillar pixels in our LFP, we achieved a maximum pixel resolution of 25,400 dots per inch. To the best of our knowledge, this pixel resolution is the highest for LFPs that have been reported so far. From the palette of 64 colours (6 bits) in Supplementary Fig. 1a, we calculated the maximum amount of information stored in our LFP to be 0.98 Megabits per  $\text{mm}^2$ . We also achieved a LFP with simultaneously high spatial resolution ( $29 - 45 \mu\text{m}$ ) and high angular resolution ( $\sim 1.6^\circ$ ). Ultimately, the highest spatial resolution is determined by the smallest centre-to-centre separation between microlenses, and the highest angular resolution is determined by the maximum density of pixels under the microlenses.

Due to the serial patterning process of our TPL system, it took about 24 hours to print our LFP with an area that spanned  $2 \text{ mm} \times 2 \text{ mm}$ . Though this process currently limits upscaling and mass production, it can be improved by using parallel processing TPL systems<sup>42,43</sup> that increase the throughput by several orders of magnitude while maintaining sub-micron features and accurate alignment between the microlenses and pixels. Sub-micron features are needed to create a high-resolution LFP, whereas accurate alignment is essential to reconstruct a clear 3D image. The microlenses and pixels of our LFP were aligned automatically in the TPL system, which eliminated the need for doing manual alignment. The fabrication process can be further optimized by using more sensitive photoresists, higher laser powers and improving the design of microlenses and pixels. As the total area of the LFP is scaled up, the design needs to consider optimal observer positions based on the *NA* of microlenses to avoid an optical problem where some parts of the image lie outside the acceptable range of viewing angles. The *NA* of a microlens is determined by its diameter and focal length. In our LFP, we set the focal length equal to the separation distance between microlenses and pixels. This separation distance also needs to be carefully designed. A larger separation distance increases the aspect ratio of the support structure, which makes it less stable and less feasible to fabricate. We suggest that the aspect ratio should

not exceed  $\sim 10:1$ , which was the case in our LFP. Conversely, a smaller separation distance would produce less saturated colours as unwanted wavelengths of light scattered from the nanopillar pixels are collected by microlenses with larger  $NA$ . Hence, the separation distance has an upper limit determined by the mechanical stability of high aspect ratio support structures and the minimum acceptable range of viewing angles. The lower limit is determined by matching the  $NA$  of microlenses with the maximum viewing angle of pixels (Fig. 2e) to avoid reducing colour saturation.

In terms of security, copying the LFP by nanoimprint lithography would be extremely difficult because the lenses shield the pixels from being moulded, which can provide a physically unclonable function for anti-counterfeiting. At the same time, the LFP is easy to observe by naked eye under ambient white light illumination and its optically variable feature can benefit security documents such as passports. The LFP does not require special glasses for viewing, nor does it require laser illumination used in conventional holograms. In terms of performance, the pixels of our LFP covered only a limited colour gamut ( $\sim 40\%$  sRGB) as they were made entirely of IP-Dip photoresist, a low refractive index material. By contrast, pixels made of high refractive index materials such as silicon can yield a much wider colour gamut<sup>19,44,45</sup> covering up to the Rec. 2020 colour space. However, the downside is that high refractive index materials also introduce stronger dispersion and reflective losses that diminish the optical performance of microlenses. Whilst more research is needed in nanoscale 3D printing of high refractive index materials<sup>46</sup>, the choice of a low refractive index material allowed the microlenses and pixels to be printed in a single process that greatly reduced the design constraints of our LFP. Another limitation is that the fabricated structures of the LFP are fragile and can be easily wiped off by hand. To protect the LFP from structural damage, we suggest keeping it inside a glass enclosure under room temperature and pressure. Nonetheless, we emphasize the main advantage of nanoscale 3D printing in creating not only high-resolution, but also fully customizable LFPs.

In the future, hyper-realistic LFPs can be created by integrating high optical performance metalenses<sup>47-50</sup> and structural colour pixels. Hyper-realistic LFPs will require a wide range of viewing angles to deliver an immersive 3D experience. This goal can be achieved by sophisticated design and fabrication of metalenses<sup>51,52</sup> that

provide large fields of view up to  $180^\circ$  and correct for field-dependent aberrations. To reduce unwanted iridescence over a wide range of viewing angles, angle-insensitive structural colour pixels<sup>53,54</sup> should also be designed and fabricated. In addition, the metalenses and structural colour pixels can be fabricated on curved substrates<sup>55</sup> instead of flat substrates. If high numerical aperture metalenses ( $NA \sim 1$ ) are combined with angle-insensitive structural colour pixels of 250 nm pitch, a hyper-realistic LFP that provides a  $\sim 180^\circ$  range of viewing angles and an angular resolution of  $0.4^\circ$  can be achieved. Hyper-realistic LFPs will find potential applications in artworks and product protection features aimed at the high-value market.

## Methods

**Simulations.** Raytracing simulation of the microlens was done in MATLAB by defining the geometric profile of the microlens and applying Snell's law at each interface (Supplementary Note 1). Electromagnetic wave simulation of the microlens and structural colour pixel was done in Lumerical FDTD Solutions by using the finite-difference time-domain method. The microlens surface was defined by diameter = 21  $\mu\text{m}$ , radius of curvature = 22  $\mu\text{m}$ , conic constant = 0. A plane wave source was launched from the convex side of the microlens and its electric field intensity distribution at the focal plane ( $z = 37 \mu\text{m}$ ) was recorded and normalized to the maximum intensity. The structural colour pixel contained an array of  $5 \times 5$  nanopillars on a glass substrate. Each nanopillar was modelled as a cylinder capped with a hemisphere, with diameter = 0.3  $\mu\text{m}$ , height = 1.2  $\mu\text{m}$  and pitch = 1  $\mu\text{m}$ , which were average values measured from the SEM images. A total-field scattered-field source was launched from the substrate side. The power transmitted into the far field was calculated within a  $16^\circ$  integration cone. The centre of the integration cone was tilted at  $0^\circ$ ,  $8^\circ$ , and  $16^\circ$  to simulate different viewing angles. The calculated spectra were normalized to a reference transmission spectrum from a control setup without the nanopillars.

**Fabrication.** A drop of IP-Dip photoresist was placed on a fused silica substrate and patterned by a Nanoscribe GmbH Photonic Professional GT system. The writing mode was set to GalvoScanMode, and the laser's power was set to 20 mW. The nanopillars of the pixels were written in PulsedMode, while the towers and microlenses were

written in ContinuousMode. After patterning, the substrate was immersed in propylene glycol monomethyl ether acetate solution for 11 mins, then in isopropyl alcohol solution for 2 mins with UV curing, and then in nonafluorobutyl methyl ether solution for 5 mins. Lastly, the substrate was dried in air.

**Imaging.** The optical microscope images in Fig. 3a – 3c were taken with a Nikon T Plan EPI SLWD 10× NA0.2 objective attached to a Nikon DS-Ri2 microscope camera. The SEM images in Fig. 3d – 3e were taken with a JEOL JSM-7600F field emission SEM system. The digital camera images in Figs. 4 – 6 were taken with a Canon EF 100 mm f/2.8 Macro USM lens mounted on a Canon EOS 5D Mark III DSLR camera set to manual exposure mode: ISO 800, f/4, 1/100 s. The colour brightness and contrast of the digital camera images were adjusted via image processing to provide a consistent appearance for presentation.

## Code availability

The code used to fabricate the light field print is available from the corresponding authors upon reasonable request.

## References

- 1 Ng, R. *Digital light field photography*. (Stanford university, 2006).
- 2 Lam, E. Y. Computational photography with plenoptic camera and light field capture: tutorial. *J. Opt. Soc. Am. A* **32**, 2021-2032 (2015).
- 3 Manuel, M.-C. & Bahram, J. Fundamentals of 3D imaging and displays: a tutorial on integral imaging, light-field, and plenoptic systems. *Adv. Opt. Photon.* **10**, 512-566 (2018).
- 4 Yoon, H. *et al.* Arrays of Lucius micropisms for directional allocation of light and autostereoscopic three-dimensional displays. *Nat. Commun.* **2**, 455 (2011).
- 5 Lippmann, G. La photographie intégrale. *C. R. Acad. Sci.* **46**, 446-451 (1908).
- 6 Woods, A., Harris, C., Leggo, D. & Rourke, T. Characterizing and reducing crosstalk in printed anaglyph stereoscopic 3D images. *Opt. Eng.* **52**, 043203 (2013).
- 7 Goh, X. M. *et al.* Three-dimensional plasmonic stereoscopic prints in full colour. *Nat. Commun.* **5**, 5361 (2014).
- 8 Lim, K. T. P., Liu, H., Liu, Y. & Yang, J. K. W. Holographic colour prints for enhanced optical security by combined phase and amplitude control. *Nat. Commun.* **10**, 25 (2019).
- 9 Xiao, X., Bahram, J., Manuel, M.-C. & Adrian, S. Advances in three-dimensional integral imaging: sensing, display, and applications [Invited]. *Appl. Opt.* **52**, 546-560 (2013).
- 10 Park, S.-g. *et al.* Recent issues on integral imaging and its applications. *J. Inf. Disp.* **15**, 37-46 (2014).
- 11 Kumar, K. *et al.* Printing colour at the optical diffraction limit. *Nat. Nanotechnol.* **7**, 557-561 (2012).

- 12 Tan, S. J. *et al.* Plasmonic color palettes for photorealistic printing with aluminum nanostructures. *Nano Lett.* **14**, 4023-4029 (2014).
- 13 Roberts, A. S., Pors, A., Albrektsen, O. & Bozhevolnyi, S. I. Subwavelength plasmonic color printing protected for ambient use. *Nano Lett.* **14**, 783-787 (2014).
- 14 Gu, Y., Zhang, L., Yang, J. K. W., Yeo, S. P. & Qiu, C.-W. Color generation via subwavelength plasmonic nanostructures. *Nanoscale* **7**, 6409-6419 (2015).
- 15 James, T. D., Mulvaney, P. & Roberts, A. The plasmonic pixel: Large area, wide gamut color reproduction using aluminum nanostructures. *Nano Lett.* **16**, 3817-3823 (2016).
- 16 Kristensen, A. *et al.* Plasmonic colour generation. *Nat. Rev. Mater.* **2**, 16088 (2016).
- 17 Miyata, M., Hatada, H. & Takahara, J. Full-color subwavelength printing with gap-plasmonic optical antennas. *Nano Lett.* **16**, 3166-3172 (2016).
- 18 Zhu, X., Vannahme, C., Højlund-Nielsen, E., Mortensen, N. A. & Kristensen, A. Plasmonic colour laser printing. *Nat. Nanotechnol.* **11**, 325-329 (2016).
- 19 Dong, Z. *et al.* Printing beyond sRGB color gamut by mimicking silicon nanostructures in free-space. *Nano Lett.* **17**, 7620-7628 (2017).
- 20 Zhu, X., Yan, W., Levy, U., Mortensen, N. A. & Kristensen, A. Resonant laser printing of structural colors on high-index dielectric metasurfaces. *Sci. Adv.* **3**, e1602487 (2017).
- 21 Liu, Y. *et al.* Structural color three-dimensional printing by shrinking photonic crystals. *Nat. Commun.* **10**, 4340 (2019).
- 22 Rezaei, S. D. *et al.* Wide-gamut plasmonic color palettes with constant subwavelength resolution. *ACS Nano* **13**, 3580-3588 (2019).
- 23 Wang, H. *et al.* Painting with hue, saturation, and brightness control by nanoscale 3D printing. Preprint at <https://arxiv.org/abs/2010.11035> (2020).
- 24 Zhang, W. *et al.* Structural multi-colour invisible inks with submicron 4D printing of shape memory polymers. *Nat. Commun.* **12**, 112 (2021).
- 25 Yasuda, S. & Shimizu, K. Pinned square lens arrays and their application to integral photography. *Jpn. J. Appl. Phys.* **52**, 06GL03 (2013).
- 26 Cote, P. F. Micro-optic security device. United States patent US8739711B2 (2014).
- 27 Jiang, H., Kaminska, B., Porras, H., Raymond, M. & Kapus, T. Microlens arrays above interlaced plasmonic pixels for optical security devices with high-resolution multicolor motion effects. *Adv. Opt. Mater.* **7**, 1900237 (2019).
- 28 Zhou, Y. *et al.* Pseudo-random arranged color filter array for controlling moiré patterns in display. *Opt. Express* **23**, 29390-29398 (2015).
- 29 Thiele, S., Arzenbacher, K., Gissibl, T., Giessen, H. & Herkommer, A. M. 3D-printed eagle eye: Compound microlens system for foveated imaging. *Sci. Adv.* **3**, e1602655 (2017).
- 30 Nawrot, M., Zinkiewicz, Ł., Włodarczyk, B. & Wasylczyk, P. Transmission phase gratings fabricated with direct laser writing as color filters in the visible. *Opt. Express* **21**, 31919-31924 (2013).
- 31 Chan, J. Y. E., Ruan, Q., Ng, R. J. H., Qiu, C.-W. & Yang, J. K. W. Rotation-selective moiré magnification of structural color pattern arrays. *ACS Nano* **13**, 14138-14144 (2019).
- 32 Chiou, P.-C. & Li, J.-H. Effects of number of lenses in microlens arrays on field of view in integral imaging systems. *Int. J. Autom. Smart Technol.* **5**, 107-111 (2015).
- 33 Okano, F., Hoshino, H., Arai, J. & Yuyama, I. Real-time pickup method for a three-dimensional image based on integral photography. *Appl. Opt.* **36**, 1598-1603 (1997).
- 34 Gissibl, T., Wagner, S., Sykora, J., Schmid, M. & Giessen, H. Refractive index measurements of photo-resists for three-dimensional direct laser writing. *Opt. Mater. Express* **7**, 2293-2298 (2017).
- 35 Mahajan, V. N. *Optical imaging and aberrations: part i. ray geometrical optics.* (SPIE, 1998).
- 36 Nair S, P., Trisno, J., Wang, H. & Yang, J. K. W. 3D printed fiber sockets for plug and play micro-optics. *Int. J. Extrem. Manuf.* **3**, 015301 (2020).

- 37 Khorasaninejad, M. *et al.* Polarization-insensitive metalenses at visible wavelengths. *Nano Lett.* **16**, 7229-7234 (2016).
- 38 Takaki, Y. High-density directional display for generating natural three-dimensional images. *Proc. IEEE* **94**, 654-663 (2006).
- 39 Jung, J.-H., Hong, K. & Lee, B. Effect of viewing region satisfying super multi-view condition in integral imaging. *SID Symp. Dig. Tech. Papers* **43**, 883-886 (2012).
- 40 Chen, C., Deng, H., Zhong, F., Ji, Q. & Li, Q. Effect of viewpoints on the accommodation response in integral imaging 3D display. *IEEE Photonics J.* **12**, 1-14 (2020).
- 41 Kim, Y. M., Choi, K.-H. & Min, S.-W. Analysis on expressible depth range of integral imaging based on degree of voxel overlap. *Appl. Opt.* **56**, 1052-1061 (2017).
- 42 Saha, S. K. *et al.* Scalable submicrometer additive manufacturing. *Science* **366**, 105-109 (2019).
- 43 Geng, Q., Wang, D., Chen, P. & Chen, S.-C. Ultrafast multi-focus 3-D nano-fabrication based on two-photon polymerization. *Nat. Commun.* **10**, 2179 (2019).
- 44 Yang, B. *et al.* Ultrahighly saturated structural colors enhanced by multipolar-modulated metasurfaces. *Nano Lett.* **19**, 4221-4228 (2019).
- 45 Yang, W. *et al.* All-dielectric metasurface for high-performance structural color. *Nat. Commun.* **11**, 1864 (2020).
- 46 Vyatskikh, A., Ng, R. C., Edwards, B., Briggs, R. M. & Greer, J. R. Additive manufacturing of high-refractive-index, nanoarchitected titanium dioxide for 3D dielectric photonic crystals. *Nano Lett.* **20**, 3513-3520 (2020).
- 47 Chen, W. T. *et al.* A broadband achromatic metalens for focusing and imaging in the visible. *Nat. Nanotechnol.* **13**, 220-226 (2018).
- 48 Chen, W. T., Zhu, A. Y., Sisler, J., Bharwani, Z. & Capasso, F. A broadband achromatic polarization-insensitive metalens consisting of anisotropic nanostructures. *Nat. Commun.* **10**, 355 (2019).
- 49 Fan, Z.-B. *et al.* A broadband achromatic metalens array for integral imaging in the visible. *Light Sci. Appl.* **8**, 67 (2019).
- 50 Lin, R. J. *et al.* Achromatic metalens array for full-colour light-field imaging. *Nat. Nanotechnol.* **14**, 227-231 (2019).
- 51 Fan, C.-Y., Lin, C.-P. & Su, G.-D. J. Ultrawide-angle and high-efficiency metalens in hexagonal arrangement. *Sci. Rep.* **10**, 15677 (2020).
- 52 Lassalle, E. *et al.* Imaging properties of large field-of-view quadratic metalenses and their applications to fingerprint detection. Preprint at <https://arxiv.org/abs/2102.07999> (2021).
- 53 Wu, Y.-K. R., Hollowell, A. E., Zhang, C. & Guo, L. J. Angle-Insensitive Structural Colours based on Metallic Nanocavities and Coloured Pixels beyond the Diffraction Limit. *Sci. Rep.* **3**, 1194 (2013).
- 54 Lee, K.-T. *et al.* Angle-Insensitive and CMOS-Compatible Subwavelength Color Printing. *Adv. Opt. Mater.* **4**, 1696-1702 (2016).
- 55 Wang, W. *et al.* Large-scale microlens arrays on flexible substrate with improved numerical aperture for curved integral imaging 3D display. *Sci. Rep.* **10**, 11741 (2020).

## Acknowledgements

We acknowledge the funding support from the National Research Foundation (NRF) Singapore, under its Competitive Research Programme award NRF-CRP20-2017-0004 and NRF Investigatorship Award NRF-NRFI06-2020-0005. J.Y.E.C. thanks Andrew Bettiol, Jay Teo and Yek Soon Lok for their mentorship.

## **Author contributions**

J.Y.E.C. did the experiments and simulations, captured the images, analysed the results, and wrote the manuscript. Q.F.R. assisted in the experiments, simulations, and analysis of results. M.H.J., H.T.W., H.W. and W.Z. assisted in the analysis of results and drawing of schematics. C.W.Q. and J.K.W.Y. supervised the research. All authors edited the manuscript.

## **Competing interests**

The authors declare no conflicts of interest.

# Supplementary information for High-resolution light field prints by nanoscale 3D printing

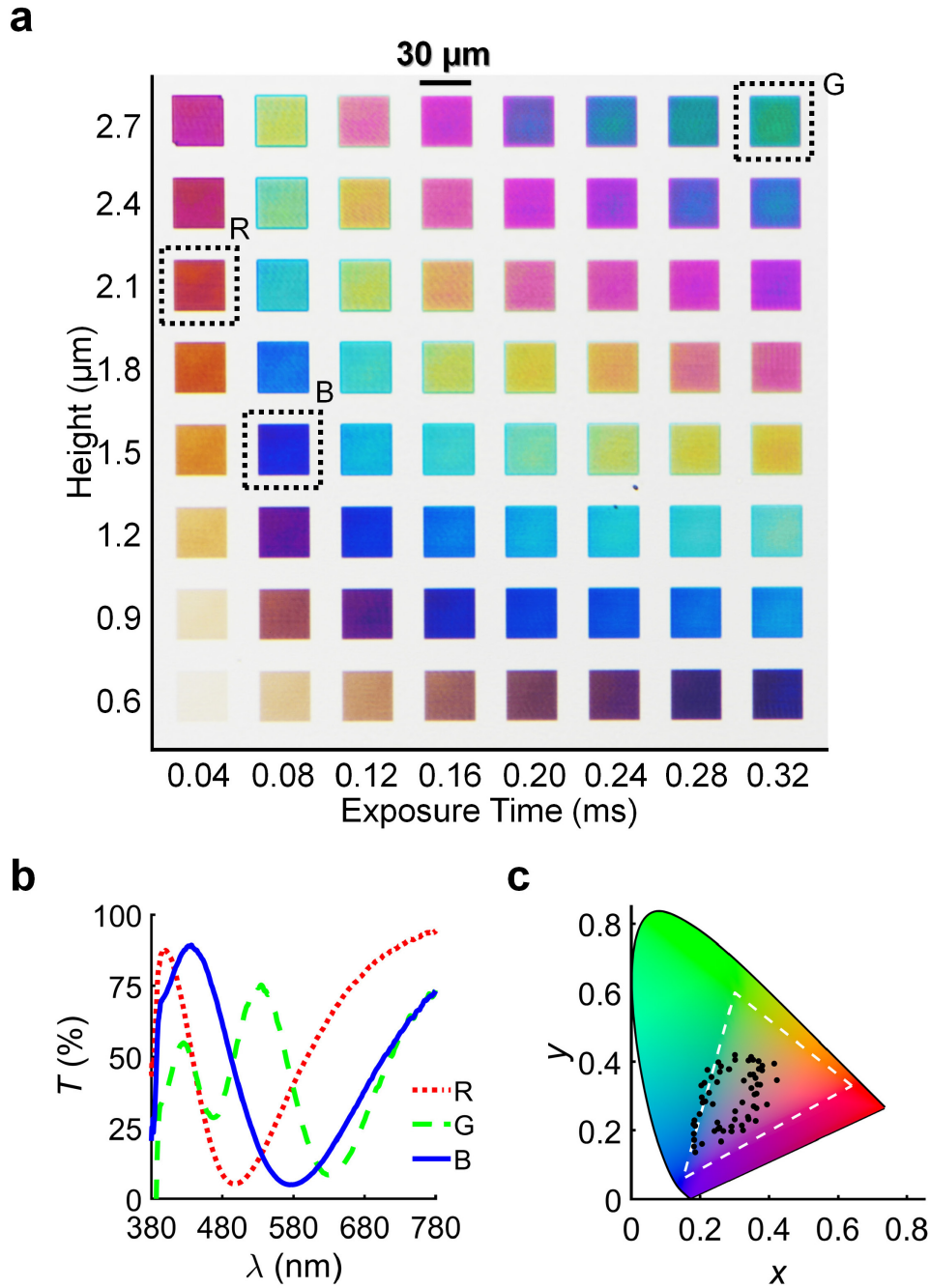
**Authors:** John You En Chan <sup>1</sup>, Qifeng Ruan <sup>1\*</sup>, Menghua Jiang <sup>2</sup>, Hongtao Wang <sup>1</sup>, Hao Wang <sup>1</sup>, Wang Zhang <sup>1</sup>, Cheng-Wei Qiu <sup>2</sup>, Joel K.W. Yang <sup>1,3\*</sup>

<sup>1</sup> Engineering Product Development, Singapore University of Technology and Design, Singapore 487372.

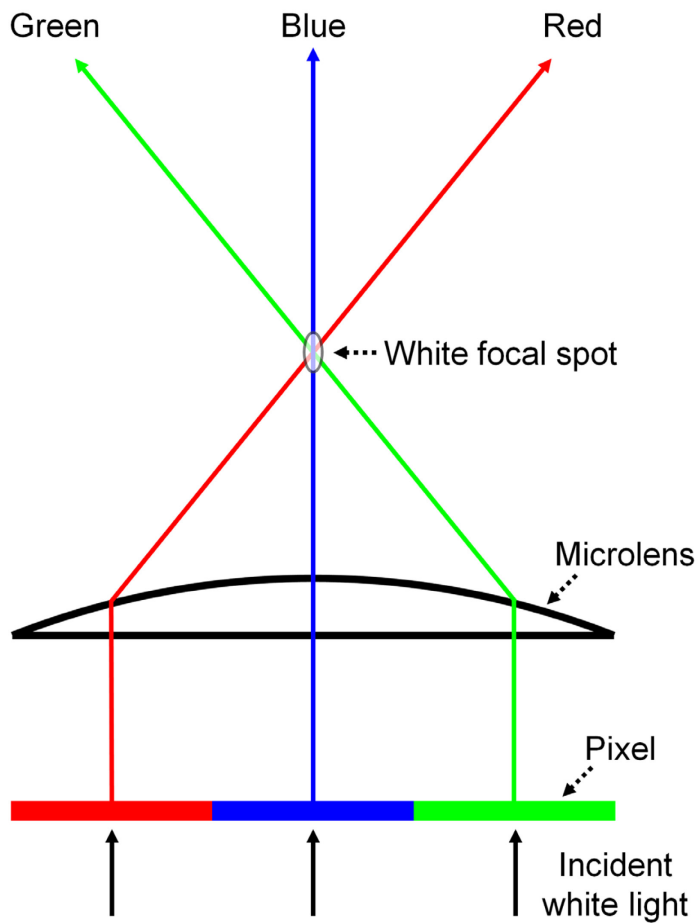
<sup>2</sup> Department of Electrical and Computer Engineering, National University of Singapore, Singapore 117583.

<sup>3</sup> Institute of Materials Research and Engineering, Singapore 138634.

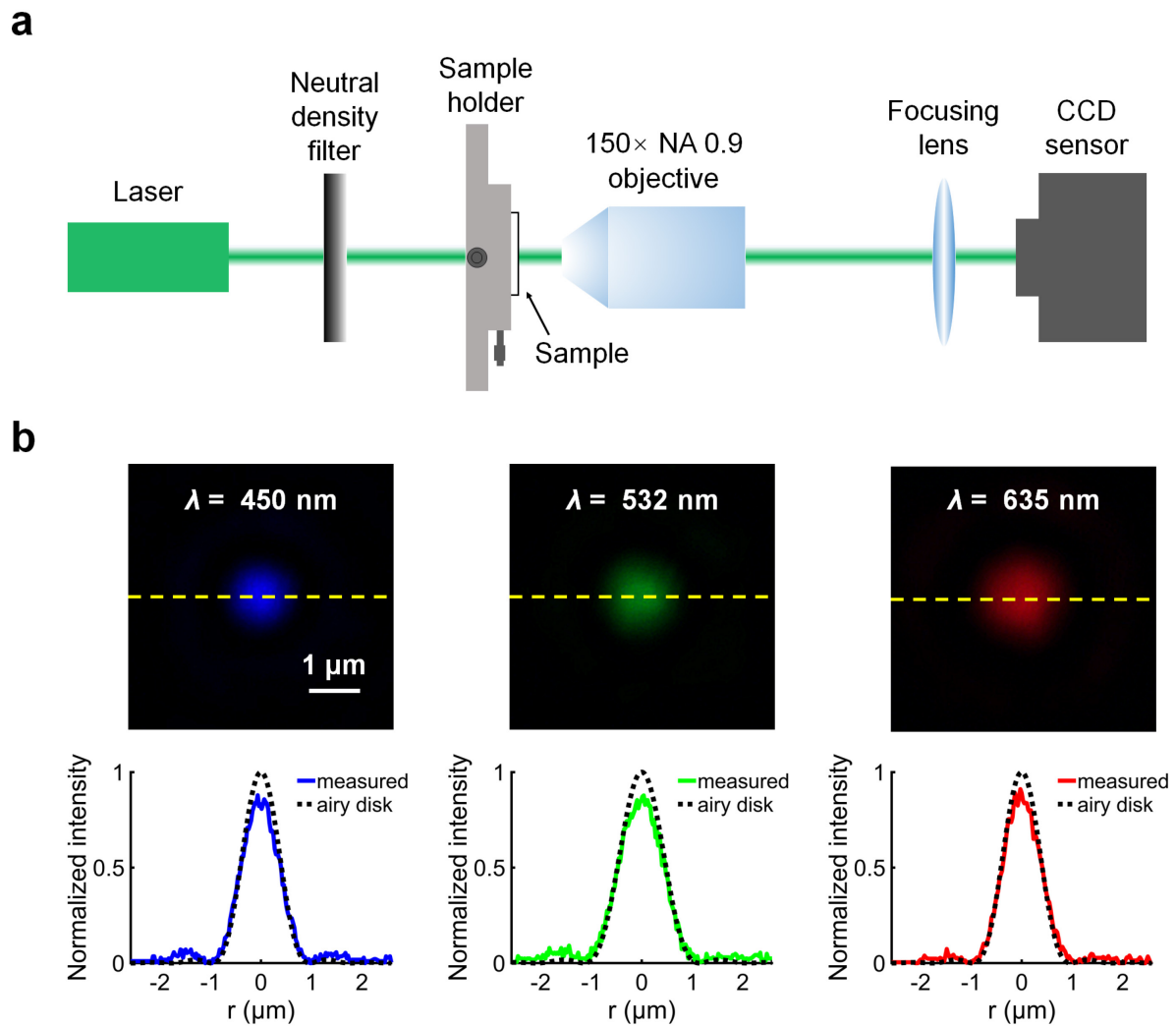
\* To whom correspondence should be addressed. Email: [qifeng\\_ruan@sutd.edu.sg](mailto:qifeng_ruan@sutd.edu.sg); [joel\\_yang@sutd.edu.sg](mailto:joel_yang@sutd.edu.sg)



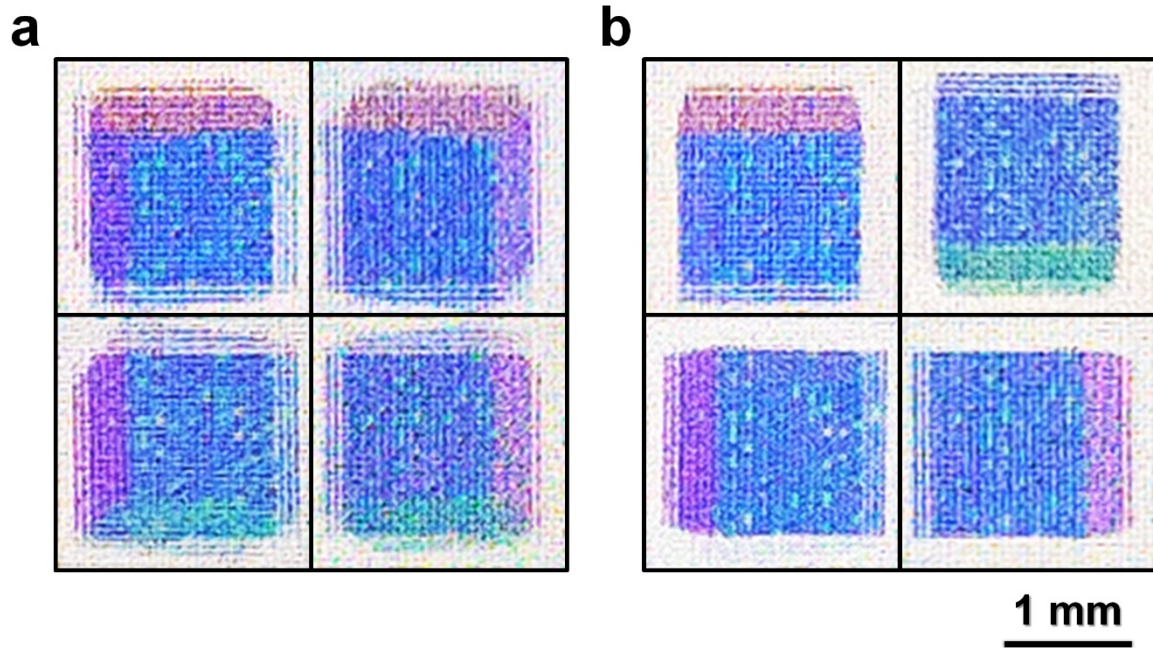
**Supplementary Figure 1.** (a) Brightfield transmission optical microscope image (taken with 10X NA 0.2 objective) showing the colour palette used to fabricate our light field print. A wide range of colour pixels was produced by varying the height of nanopillars in each pixel and the laser's exposure time per exposed voxel. The laser's power was set to 20 mW. (b) Experimentally measured transmittance spectra for pixels labelled R, G and B. (c) The CIE  $xy$  coordinates of all pixels were calculated and mapped onto the chromaticity diagram, for CIE 1931 2° Standard Observer and D65 illuminant. The sRGB colour space is outlined by the white dashed triangle.



**Supplementary Figure 2.** Schematic illustrating the colour-mixing effect in a display unit that comprises a microlens above a group of red, blue and green pixels with equal areas. Normally incident light rays from the colour pixels are focused by the microlens into a white focal spot above the display unit. Beyond the focal spot, the colour of each pixel is observed in the far-field at the corresponding viewing angle.

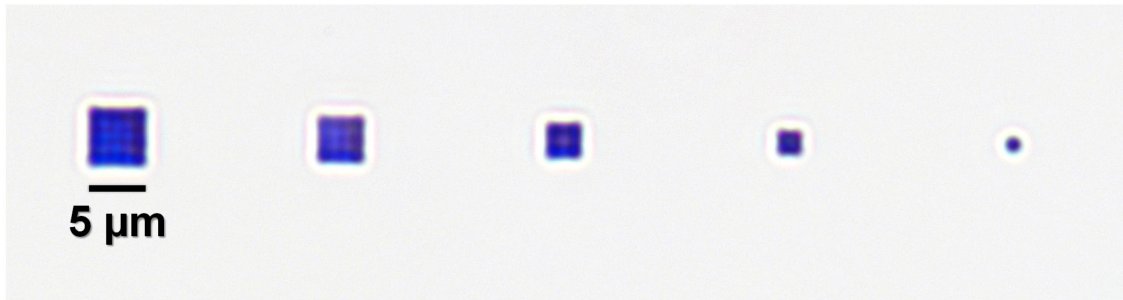


**Supplementary Figure 3.** (a) Side-view schematic of the laser setup used to capture focal spot images of a fabricated microlens. (b) (Top) Focal spot images for wavelengths  $\lambda = \{450, 532, 635\}$  nm. The centre horizontal slices of the focal spot images are indicated by the yellow dashed line. (Bottom) Measured intensity distributions of the horizontal slices normalized to an ideal Airy disk function for the respective wavelengths.

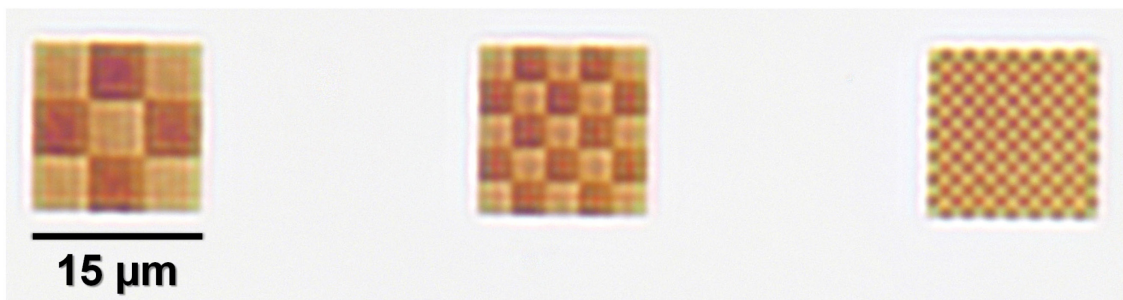


**Supplementary Figure 4.** Digital camera images of crosstalk between viewpoints. **(a)** Crosstalk in the diagonal direction. **(b)** Crosstalk in the horizontal and vertical directions.

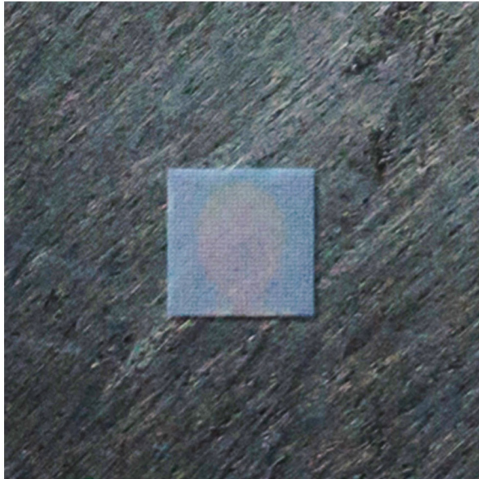
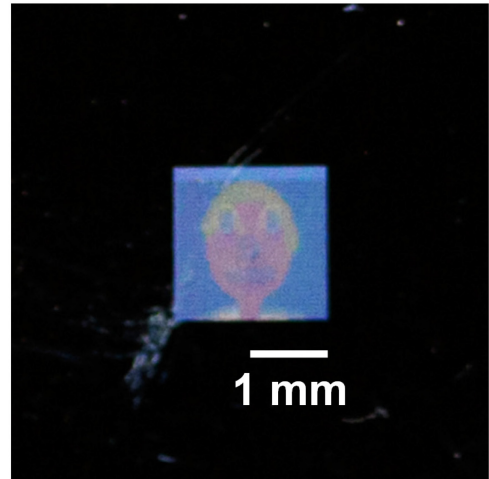
**a**



**b**



**Supplementary Figure 5.** Brightfield transmission optical microscope images (taken with 50X NA 0.4 objective) showing consistent appearance of pixel colour and contrast as the pixel size is reduced. **(a)** From left to right, the pixel size is gradually reduced from  $5 \times 5$  nanopillars to only a single nanopillar. **(b)** Checkerboard patterns of alternating light and dark colour pixels. From left to right, the pixel size in each checkboard is reduced from  $5 \times 5$  nanopillars to  $3 \times 3$  nanopillars to only a single nanopillar.

**a****b**

**Supplementary Figure 6.** Appearance of the light field print in reflection mode, where the light source and observer are on the same side as the substrate. **(a)** A matte background was placed beneath the substrate. **(b)** An aluminium mirror was placed beneath the substrate.

### Supplementary Note 1 – Geometric equations for raytracing through a lens<sup>1</sup>

Ignoring higher order terms, the sag  $z$  of a rotationally symmetric lens is expressed in Equation S1:

$$z(x, y) = \frac{x^2 + y^2}{R \left( 1 + \sqrt{1 - (1 + K) \frac{x^2 + y^2}{R^2}} \right)} + \dots \quad (\text{S1})$$

where  $(x, y, z)$  are the cartesian coordinates of the lens surface,  $R$  is the radius of curvature at the lens vertex, and  $K$  is the conic constant. We set  $K = 0$  (spherical case) and  $R = 22 \mu\text{m}$ .

Due to the rotational symmetry of the lens, analysis of the lens profile is simplified by considering only its sagittal cross-section ( $y = 0$ ). On this plane, the angle  $\sigma$  that the normal of the lens surface makes with the optical axis is expressed in Equation S2:

$$\tan \sigma = \frac{\partial s}{\partial x} = \frac{x}{R(1 + \varepsilon)} \left( 2 + \frac{(1 + K)(x^2 + y^2)}{\varepsilon(1 + \varepsilon)R^2} \right) + \dots \quad (\text{S2})$$

where  $\varepsilon = \sqrt{1 - (1 + K) \frac{x^2 + y^2}{R^2}}$ .

Once the normal of the lens surface is known, rays are traced through the lens by applying Snell's Law, which is expressed in Equation S3.

$$n_1 \sin \theta_1 = n_2 \sin \theta_2 \quad (\text{S3})$$

where  $n_1$  and  $n_2$  are the refractive index of the first medium and second medium respectively,  $\theta_1$  is the angle of incidence, and  $\theta_2$  is the angle of refraction.

## Supplementary Note 2 – Calculation of CIE XYZ and xy coordinates<sup>2</sup>

The CIE tristimulus values ( $X$ ,  $Y$ ,  $Z$ ) are expressed in Equations S4 – S7:

$$X = k \sum_{380}^{780} T(\lambda)S(\lambda)\bar{x}(\lambda)\Delta\lambda \quad (\text{S4})$$

$$Y = k \sum_{380}^{780} T(\lambda)S(\lambda)\bar{y}(\lambda)\Delta\lambda \quad (\text{S5})$$

$$Z = k \sum_{380}^{780} T(\lambda)S(\lambda)\bar{z}(\lambda)\Delta\lambda \quad (\text{S6})$$

where

$$k = 100 / \sum_{380}^{780} S(\lambda)\bar{y}(\lambda)\Delta\lambda \quad (\text{S7})$$

$k$  is the normalizing factor,  $T(\lambda)$  is the transmittance of the pixel,  $S(\lambda)$  is the relative spectral power of a CIE standard illuminant,  $\bar{x}(\lambda)$ ,  $\bar{y}(\lambda)$  and  $\bar{z}(\lambda)$  are the colour matching functions of a CIE standard observer, and  $\Delta\lambda$  is the wavelength measurement interval.

The CIE chromaticity coordinates ( $x$ ,  $y$ ) are then calculated from Equations S8 – S9:

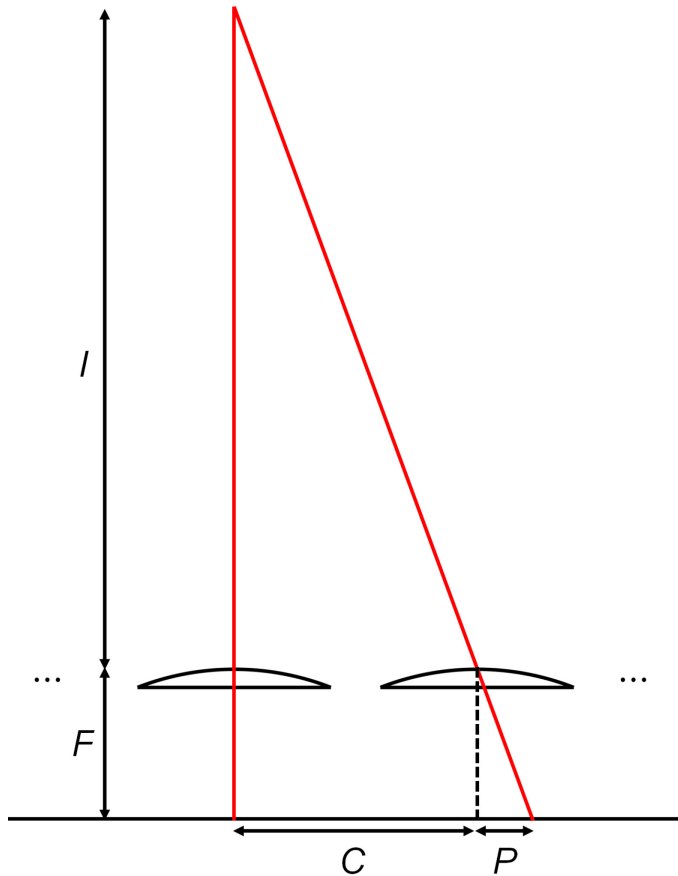
$$x = \frac{X}{X + Y + Z} \quad (\text{S8})$$

$$y = \frac{Y}{X + Y + Z} \quad (\text{S9})$$

### Supplementary Note 3 – Calculation of maximum image depth<sup>3</sup>

In our light field print (LFP), the microlenses have centre-to-centre separation  $C$  and focal length  $F$ , whereas the pixels have pixel pitch  $P$ . By using similar triangles and the paraxial approximation, the maximum image depth  $I$  is expressed in Equation S10:

$$I = \frac{CF}{P} \quad (\text{S10})$$



## Supplementary References

- 1 Mikš, A., Novák, P. & Novák, J. Calculation of aberration and direction of a normal to aspherical surface. *Opt. Laser Technol.* **45**, 708-712 (2013).
- 2 ASTM International. Standard Practice for Computing the Colors of Objects by Using the CIE System. ASTM E308-01 (2001).
- 3 Kim, Y. M., Choi, K.-H. & Min, S.-W. Analysis on expressible depth range of integral imaging based on degree of voxel overlap. *Appl. Opt.* **56**, 1052-1061 (2017).